

1 Supplement for

## 2 **Role of black carbons mass size distribution in the direct aerosol radiative forcing**

3 Gang Zhao<sup>1</sup>, Jiangchuan Tao<sup>2</sup>, Ye Kuang<sup>2</sup>, Chuanyang Shen<sup>1</sup>, Yingli Yu<sup>1</sup>, Chunsheng Zhao<sup>1\*</sup>

4 1 Department of Atmospheric and Oceanic Sciences, School of Physics, Peking University, 100871  
5 Beijing, China

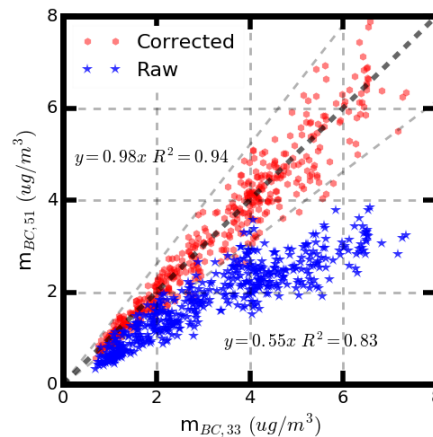
6 2 Institute for Environmental and Climate Research, Jinan University, 511443 Guangzhou, China

### 7 **1. Correcting the AE51**

8 Fig. S1 showed the results of the loading effect corrections. At the beginning of the field  
9 experiment, parallel measurement of  $m_{BC}$  by AE51 and AE33 was conducted. Before corrections, the  
10 measured  $m_{BC}$  by AE51 and AE33 showed significant discrepancy with each other with slope and  $R^2$   
11 equaling 0.55 and 0.83. However, the  $m_{BC}$  measured by AE33 and by AE51 with loading effects  
12 corrections showed good consistency in trends and magnitudes with slope and  $R^2$  of 0.98 and 0.94  
13 respectively. These results demonstrated that the loading effects corrections of  $m_{BC}$  from AE51 were  
14 essential and the value of  $m_{BC}$  from AE33 can be used as a reference for the measured BCPMSD.

15

16



17

18 **Figure S1.** Comparison between the  $m_{BC}$  measured by AE51 and AE33. The blue stars and the red  
19 dots represents uncorrected and corrected  $m_{BC}$  of AE51 respectively.

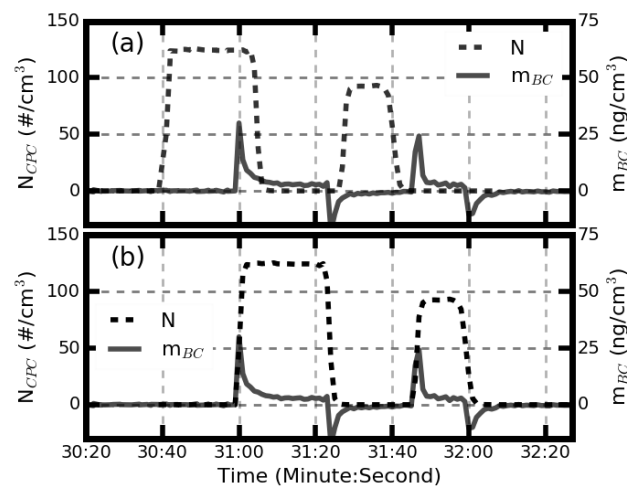
20

### 21 **2. Time correction**

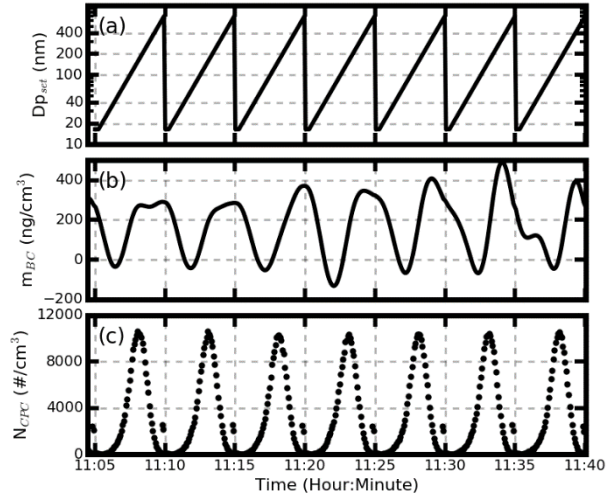
22 There were two reasons that can lead to this difference: firstly, the time of the AE51 system and

23 the computer that controls the CPC cannot be synchronized all the time; secondly, there existed a  
24 difference in the plumbing delay time, which was the time required for particles to flow through the  
25 tubing interconnecting the DMA and CPC or AE51, and arrive at the detector. To sum up, the  
26 synchronization of the time reported by CPC and AE51 was necessary.

27 Time synchronization was conducted by measuring the time lag of the signal pulses from the  
28 DMA to CPC and AE51. The signal pulses resulted from the sudden change of the aerosol diameter  
29 scanned by DMA. Details of the method were shown below. In fig. S2, the black solid line gave the  
30 time series of the measured  $m_{BC}$  by AE51. The dotted lines gave the time series of the aerosol  
31 number counted by CPC of (a) unsynchronized and (b) synchronized. In the beginning, the scan  
32 diameter of the DMA was set to be less than 13nm and the values measured by AE51 and CPC are  
33 nearly zero. The values get a step jump and a step drop when changing the scan diameter up to about  
34 200nm and down back to less than 13nm. About 15s later, these procedures were conducted once again.  
35 From fig. S2(a) and fig. S2(b), the lag time of the AE51 and CPC were determined to be 20s by  
36 matching the pulse signals.



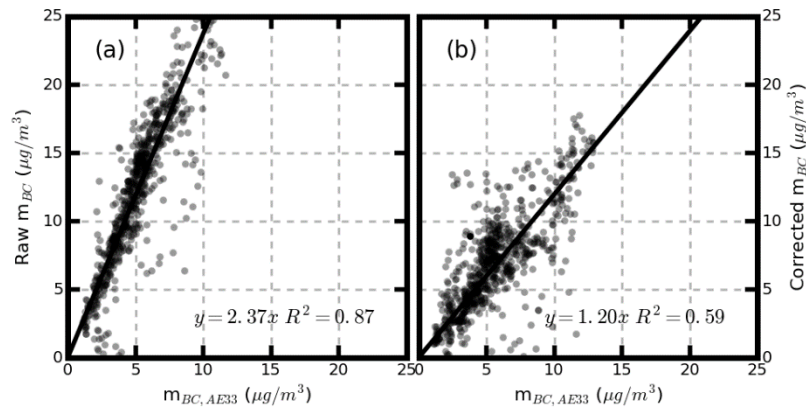
37  
38 **Figure S2.** An example of time synchronization processing, (a) for unsynchronized and (b) for  
39 synchronized. The dotted line is the aerosol number concentration time series counted by CPC. The  
40 black solid line is the BC mass concentration measured by AE51.  
41 **3. Time series diagram of scanned aerosol diameters, measured  $m_{BC}$  and the aerosol number**  
42 **concentrations**



43

44 **Figure S3** (a) the diameters of the aerosols that pass through the DMA (b) The  $m_{BC}$  values measured  
 45 by AE51, (c) the aerosol number concentrations measured by CPC.

46 **4 Validation of the multiple charging corrections**



47

48 **Figure S4.**  $m_{BC}$  measured by AE33 versus  $m_{BC}$  integrated from AE51 of (a) uncorrected BCPMSD,  
 49 (b) corrected BCPMSD.

50

51 **5 Estimate the DARF**

52 DARF is defined as the difference between radiative flux at the TOA under present aerosol  
 53 conditions and aerosol-free conditions:

$$54 \quad \text{DARF} = (f_a \downarrow - f_a \uparrow) - (f_m \downarrow - f_m \uparrow) , \quad (21)$$

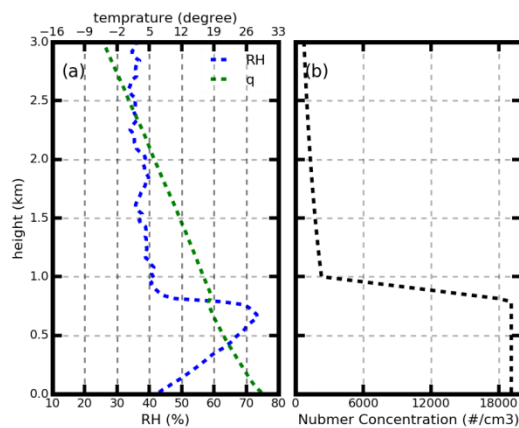
55 Where  $f_a \downarrow$  is the downward radiative irradiance and  $f_a \uparrow$  is the outward radiative irradiance under  
 56 given aerosol distributions;  $(f_a \downarrow - f_a \uparrow)$  is the downward radiative irradiance flux with given aerosol  
 57 distributions and  $(f_m \downarrow - f_m \uparrow)$  is the radiative irradiance flux under aerosol free conditions. The  
 58 wavelengths for irradiance range from 0.25 to 4  $\mu\text{m}$ .

59 Input data for the SBDART are listed below. Vertical profiles of the aerosol optical properties,  
60 which include the aerosol extinction coefficient ( $\sigma_{\text{ext}}$ ), aerosol single scattering albedo (SSA) and  $g$   
61 with a height resolution of 50 m, come from the parameterization of aerosol vertical distributions (as  
62 shown in fig. S4 and the next paragraph) and the results of the Mie model.

63 Liu et al. (2009) studied vertical profiles of aerosol total number concentration ( $N_a$ ) with aircraft  
64 measurements, and derived a parameterized vertical distribution. In this scheme,  $N_a$  is constant in the  
65 mixed layer, with a transition layer where it linearly decreases and an exponential decrease of  $N_a$   
66 above the transition layer. The same parameterized scheme proposed by Liu et al. (2009) is adopted by  
67 this study as shown in fig. S4 (b). Both the study of Liu et al. (2009) and Ferrero et al. (2010) manifest  
68 that the dry aerosol PNSD in the mixed layer varies little. The shape of the dry aerosol PNSD is  
69 assumed constant with height, which means that aerosol PNSD at different heights divided by  $N_a$  give  
70 the same normalized PNSD.

71 As for the BC vertical distribution, Ferrero et al. (2011) and Ran et al. (2016) demonstrate that BC  
72 mass concentration in the mixed layer remains relatively constant and decreases sharply above the  
73 mixed layer. According to this, the parameterization scheme of BC vertical distribution is assumed to  
74 be the same as that of aerosol. The shape of the size-resolved BC mass concentration distribution is  
75 also assumed to be the same as that at the surface.

76



77

78 **Figure S5.** The mean RH, temperature, and aerosol number concentration profiles.

79

80 Atmospheric gas and meteorological parameter profiles come from the mean results of the  
81 radiosonde observations at the Meteorological Bureau of Beijing (39°48' N, 116°28' E), which include

82 profiles for water vapor, pressure and temperature during the summer (Supplementary S5). With the  
 83 vertical distribution of aerosol PNSD and BCMSD, the aerosol optical properties at a given height can  
 84 be calculated based on the method of S6. Surface albedo values are obtained from the Moderate  
 85 Resolution Imaging Spectroradiometer (MODIS) V005 Climate Modeling Grid (CMG) Albedo  
 86 Product (MCD43C3) during March, 2017 of Beijing, where the field campaign is conducted. The  
 87 remaining input data for the SBDART are set to their default values.

88

## 89 **6. Calculate the aerosol optical profiles under the given RH profile**

90 The aerosol hygroscopic growth is taken into consideration when calculate the aerosol optical  
 91 properties under the given RH. The  $\kappa$ -Köhler theory (Petters and Kreidenweis, 2007) is widely used to  
 92 describe the hygroscopic growth of aerosol particles by using a single aerosol hygroscopic growth  
 93 parameter ( $\kappa$ ) and the  $\kappa$ -Köhler equation, which is shown as

$$94 \quad \frac{RH}{100} = \frac{gf^3 - 1}{gf^3 - (1 - \kappa)} \cdot \exp\left(\frac{4\sigma_{s/a}M_{water}}{R \cdot T \cdot D_d \cdot gf \cdot \rho_w}\right), \quad (1)$$

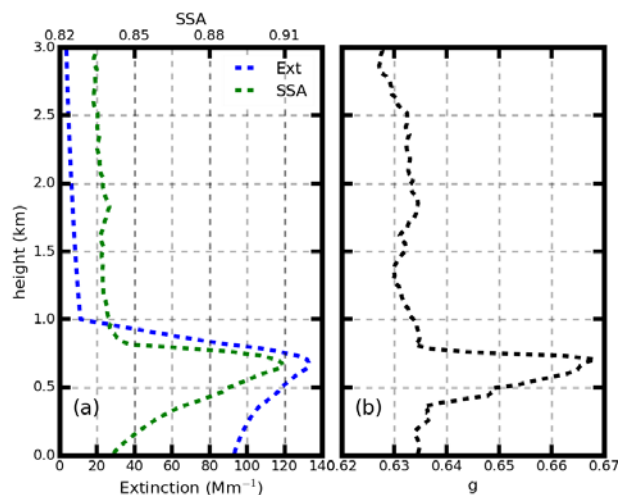
95 where  $D_d$  is the dry particle diameter;  $gf(RH)$  is the aerosol growth factor, which is defined as the  
 96 ratio of the aerosol diameter at a given RH and the dry aerosol diameter ( $D_{RH}/D_d$ );  $T$  is the  
 97 temperature;  $\sigma_{s/a}$  is the surface tension of the solution;  $R$  is the universal gas constant and  $\rho_w$  is the  
 98 density of water. The aerosol hygroscopic growth parameter  $\kappa$  can be further used to investigate the  
 99 influence of aerosol hygroscopic growth on aerosol optical properties (Tao et al., 2014; Kuang et al.,  
 100 2015; Zhao et al., 2017) and aerosol liquids water contents (Bian et al., 2014).

101 The  $\kappa$ -Köhler theory and the Mie scattering model are combined to calculate aerosol extinction  
 102 coefficient, aerosol single scattering albedo and aerosol asymmetry factor under different RH  
 103 conditions. The real time  $\kappa$ , which is derived from the measurement of  $f(RH)$ , is used to account for  
 104 aerosol hygroscopic growth. For each RH value, the  $gf$  can be calculated based on equation (1). The  
 105 corresponding ambient aerosol PNSD at a given RH can be determined too. The refractive index ( $\tilde{m}$ ),  
 106 which accounts for water content in the particle, is derived as a volume mixture between the dry  
 107 aerosol and water (Wex et al., 2002):

$$108 \quad \tilde{m} = f_{v,dry} \tilde{m}_{aero,dry} + (1 - f_{v,dry}) \tilde{m}_{water} \quad (2)$$

109 where  $f_{v,dry}$  is the ratio of the dry aerosol volume to the total aerosol volume under a given RH  
 110 condition;  $\tilde{m}_{aero,dry}$  is the refractive index for dry ambient aerosols and  $\tilde{m}_{water}$ , the refractive index

111 of water, is  $1.33 \times 10^{-7}$ . Then, the corresponding aerosol optical properties under the given RH and  
 112 PNSD can also be calculated. Finally, the aerosol optical profiles can be calculated. Fig. S5 shows one  
 113 of the calculated aerosol optical profiles.



114 **Figure S6.** The calculated profiles of the aerosol extinction coefficient, aerosol single scattering  
 115 albedo and the aerosol asymmetry factor.

116

117

118 Bian, Y. X., Zhao, C. S., Ma, N., Chen, J., and Xu, W. Y.: A study of aerosol liquid water content based  
 119 on hygroscopicity measurements at high relative humidity in the North China Plain, *Atmospheric*  
 120 *Chemistry and Physics*, 14, 6417-6426, 10.5194/acp-14-6417-2014, 2014.

121 Ferrero, L., Perrone, M. G., Petraccone, S., Sangiorgi, G., Ferrini, B. S., Lo Porto, C., Lazzati, Z.,  
 122 Cocchi, D., Bruno, F., Greco, F., Riccio, A., and Bolzacchini, E.: Vertically-resolved particle size  
 123 distribution within and above the mixing layer over the Milan metropolitan area, *Atmospheric*  
 124 *Chemistry and Physics*, 10, 3915-3932, 2010.

125 Ferrero, L., Mocnik, G., Ferrini, B. S., Perrone, M. G., Sangiorgi, G., and Bolzacchini, E.: Vertical  
 126 profiles of aerosol absorption coefficient from micro-Aethalometer data and Mie calculation over  
 127 Milan, *Science of the Total Environment*, 409, 2824-2837, 2011.

128 Kuang, Y., Zhao, C. S., Tao, J. C., and Ma, N.: Diurnal variations of aerosol optical properties in the  
 129 North China Plain and their influences on the estimates of direct aerosol radiative effect, *Atmos. Chem.*  
 130 *Phys.*, 15, 5761-5772, 10.5194/acp-15-5761-2015, 2015.

131 Liu, P., Zhao, C., Zhang, Q., Deng, Z., Huang, M., Xincheng, M. A., and Tie, X.: Aircraft study of

132 aerosol vertical distributions over Beijing and their optical properties, *Tellus Series B-Chemical &*  
133 *Physical Meteorology*, 61, 756–767, 2009.

134 Petters, M. D., and Kreidenweis, S. M.: A single parameter representation of hygroscopic growth and  
135 cloud condensation nucleus activity, *Atmos. Chem. Phys.*, 7, 1961-1971, 10.5194/acp-7-1961-2007,  
136 2007.

137 Ran, L., Deng, Z., Xu, X., Yan, P., Lin, W., Wang, Y., Tian, P., Wang, P., Pan, W., and Lu, D.: Vertical  
138 profiles of black carbon measured by a micro-aethalometer in summer in the North China Plain,  
139 *Atmospheric Chemistry and Physics*, 16, 10441-10454, 10.5194/acp-16-10441-2016, 2016.

140 Tao, J. C., Zhao, C. S., Ma, N., and Liu, P. F.: The impact of aerosol hygroscopic growth on the  
141 single-scattering albedo and its application on the NO<sub>2</sub> photolysis rate coefficient, *Atmos. Chem. Phys.*,  
142 14, 12055-12067, 10.5194/acp-14-12055-2014, 2014.

143 Wex, H., Neususs, C., Wendisch, M., Stratmann, F., Koziar, C., Keil, A., Wiedensohler, A., and Ebert,  
144 M.: Particle scattering, backscattering, and absorption coefficients: An in situ closure and sensitivity  
145 study, *J Geophys Res-Atmos*, 107, 10.1029/2000jd000234, 2002.

146 Zhao, G., Zhao, C., Kuang, Y., Tao, J., Tan, W., Bian, Y., Li, J., and Li, C.: Impact of aerosol  
147 hygroscopic growth on retrieving aerosol extinction coefficient profiles from elastic-backscatter lidar  
148 signals, *Atmos. Chem. Phys. Discuss.*, 2017, 1-24, 10.5194/acp-2017-240, 2017.

149